H2 production by formic acid decomposition on ceria-modified Ru/TiO2 catalysts under dual photonic/thermal excitation

José Montes-Monroy, Ramón Manzorro, Laura Valenzuela, Javier Ivanez, José Pérez-Omil, Nicolas Keller

H_2 production by formic acid decomposition on ceria-modified Ru/TiO_2 catalysts under dual photonic/thermal excitation

José M. Montes-Monroy,[a] Ramón Manzorro,[a,*] Laura Valenzuela,[b] Javier Ivanez,[b] José A. Pérez-Omil,[a] Nicolas Keller[b,*]

*Corresponding authors: Nicolas Keller (nkeller@unistra.fr);

Ramón Manzorro (ramon.manzorro@gm.uca.es)

[a] Departamento de Ciencias de los Materiales e Ingeniería Metalúrgica y Química Inorgánica, Facultad de Ciencias, Universidad de Cádiz, Spain.

[b] Institut de Chimie et Procédés pour l'Energie, l'Environnement et la Santé (ICPEES), CNRS/Strasbourg University, 25 rue Becquerel, 67087 Strasbourg, France.

KEYWORDS

Photo-assisted synthesis ; Ru nanoclusters ; CeO_2/TiO_2 ; Dual photonic/thermal excitation ; H_2 production ; Formic acid decomposition

ABSTRACT

Formic acid is a high-prospect energy carrier of sustainable H_2 and can also favorably supply sustainable H_2 to hydrogenation catalysts in replacement of external pressurized H_2. A solar photon-assisted synthesis method was successfully implemented for decorating a ceria-modified TiO_2 support with ultra-dispersed Ru nanoclusters with a large fraction of low atomicity species and Ru single atoms. Adding ceria to the TiO_2 support at a quarter of the theoretical monolayer is a suited surface modification for partially reducing the detrimental intrinsic activity of the bare TiO_2 surface for the dehydration of formic acid, what allows the undesired formation of CO to be mitigated and higher selectivities to H_2 to be achieved when using the $Ru/CeO_2/TiO_2$ catalyst. The dual (combined) photonic/thermal excitation of the $Ru/CeO_2/TiO_2$ catalyst boosted the H_2 production rate and allowed the dehydrogenation reaction to be conducted at a lower temperature compared to the dark conditions, for instance with a 80°C downshift at 190°C, what corresponded to a 42% relative gain compared to the dark conditions. Advanced electron microscopy characterization has been crucial to unveil the atomic-level nature of the $Ru/CeO_2/TiO_2$ photo-thermo catalyst, bringing to light the presence of ultra-dispersed metallic Ru nanoclusters, both (i) decorating nanometric size flat CeO_2 nanoparticles interfaced in epitaxy with high-index TiO_2 facets, and (ii) being homogeneously distributed over the TiO_2 surface in close vicinity with low atomicity CeO_2 species.

1. Introduction

Sustainable chemistry relies on reactions with reduced environmental impact and minimal energy demand, generally driven by the integration of renewable energies in the chemical processes. Albeit intermittent, solar energy is an ideal and abundant renewable energy source to be integrated into catalytic processes to make them more sustainable and cost-effective [1]. Progresses in heterogeneous catalysis were achieved in the last decades while considering both thermal and photonic excitations as distinct strategies for driving reactions selectively and with high efficiency.

However, much hope aroused recently from the evidence of cooperative effects between thermal and photonic excitations in heterogeneous catalysis for a large span of reactions. This approach is driven by the necessity to speed up reaction rates for shortening the processing durations under given reaction conditions, to soften the reaction conditions and in particular the temperature while achieving similar yields, or to orientate the reaction selectivity by allowing new pathways through new transition states of lower potential energy [2–5].

Recently, Ivanez et al. demonstrated the benefit of applying a dual thermal/photonic excitation to a Ru/TiO_2 catalyst for boosting the dehydrogenation of gaseous formic acid to H_2 [6], for which small size Ru species are reported to be efficient catalysts [7,8]. Formic acid being a primary side-product of the cellulose hydrolytic conversion in the processing of bio-resources [9–11], this high-interest reaction relates mainly to two important applications. First, it is a key-reaction in the context of energy storage, as formic acid is a high-prospect energy carrier of sustainable hydrogen [12]. Second, this reaction can be used favorably in a H-transfer (H donor-mediated) strategy of sustainable internal H_2 supply aiming at superseding the use of external pressurized H_2 in catalytic hydrogenations for improving the sustainability of hydrogenation processes [13–15]. However, the dehydrogenation of formic acid into H_2 and

CO_2 (Eq. 1) is known to compete with its dehydration into CO and H_2O (Eq. 2), which generates unwanted poisoning CO [16]:

$$HCOOH \rightarrow H_2 + CO_2 \quad (1)$$

$$HCOOH \rightarrow CO + H_2O \quad (2)$$

In addition to boost the H_2 production rate and to drive the dehydrogenation reaction at a lower temperature without being detrimental to the H_2 production level, the dual-mode excitation of the Ru/TiO_2 catalyst was observed to increase the selectivity to H_2. However, we also showed that the performances remained limited by the intrinsic ability of the TiO_2 semiconductor support to catalyze the adverse dehydration of formic acid to CO that is poisoning the Ru nanoparticles.

TiO_2 being a high-prospect support for Ru nanoparticles that allows the implementation of an H donor-mediated strategy for catalytic hydrogenation reactions with internal H_2 supply [14], modifying the TiO_2 surface is a worthy approach for mitigating the CO formation. Ceria stands out as a promising modifier given its ability to be used as non-stoichiometric oxide support [17,18] and to create oxygen vacancies at low/mild temperature under reducing atmospheres [19]. Thereby, we investigate here to which extent the addition of ceria to the TiO_2 support is a suited surface modification strategy for mitigating the undesired side-formation of CO in the H_2 production by gas-phase dehydrogenation of formic acid under dual photonic/thermal excitation.

2. Experimental

2.1 Materials and synthesis methods

Anatase–rutile mixed phase Aeroxide© TiO_2-P25 with a BET specific surface area of 51 m^2/g and mean crystallite sizes of 18 nm and 35 nm for anatase and rutile phases, respectively, was supplied by Evonik Industries AG (Germany) and used as support without any further modification.

The CeO_2/TiO_2-P25 support was prepared by incipient wetness impregnation (IWI). The incipient volume 2.1 mL of a 0.15M $Ce(NO_3)_3$ aqueous solution prepared by dissolving cerium nitrate hexahydrate (99.5%, Alfa Aesar) in milli-Q water, was added dropwise onto 2.0 g of the support with thorough physical mixing, ideally covering the surface of the TiO_2-P25. Then, the sample was dried at 90ºC for 24 h, submitted to a calcination treatment in a muffle oven at 500ºC for 30 min and finally passed through a 75 μm pore sized sieve. The nominal amount of CeO_2 was selected as being a quarter of the theoretical monolayer, which was calculated from the BET specific area of the host TiO_2 and the average number of Ce cations per nm^2 (7.5 Ce cations/nm^2), estimated from the most probably exposed crystal facets in the CeO_2 fluorite structure. The nominal amount of CeO_2 corresponded to 2.7 wt.% relatively to the CeO_2/TiO_2-P25 support.

The TiO_2-P25 and CeO_2/TiO_2-P25, in the following TiO_2 and CeO_2/TiO_2, supported Ru photo-thermo catalysts were prepared with a nominal Ru wt.% content of 0.5% according to a photon-assisted synthesis method using ruthenium(III) chloride trihydrate ($RuCl_3$ x H_2O, 40% Ru wt.) from Sigma-Aldrich as precursor. The Ru precursor (12.5 mg) was dissolved under stirring in 10 mL of methanol for 12 h, and later 1 mL aliquot was taken to prepare a 100 mL 10% v/v methanol/aqueous solution with a final concentration of 12.5 mg/L. The support was dispersed in this solution at a concentration of 1 g/L under stirring (350 rpm) for 1 h in order to ensure the establishment of the dark adsorption/desorption equilibrium, and the suspension was further exposed under stirring to a 500 W/m^2 solar-light irradiation within an

ATLAS Suntest XLS+ reaction chamber (Xenon arc lamp NXE 2201). At each time interval, a 5 mL sample was taken and filtered through a 0.20 μm porosity filter (Aireka Cells) in order to remove any powder. The reaction was monitored by UV-Vis spectrophotometry using a UV-1600 PC spectrophotometer (VWR) by following the disappearance of the main absorption peak at $\lambda = 324$ nm for the Ru precursor. After completion of the process, the suspended catalyst was recovered by vacuum filtration, washed several times with milli-Q water, and dried in an oven at 100ºC for 1 h.

2.2 Characterization techniques

Carbon coated copper grids were used to deposit the powdery catalysts in order to be characterized by using Scanning/Transmission Electron Microscopy techniques, using a double aberration-corrected FEI Titan Cubed Themis 60-300 working at 300 KV. Sub-angstrom resolution High Angle Annular Dark Field (HAADF) images were registered: spherical aberration Cs, 0.001 mm; fifth-order spherical aberration, 5 mm; defocus, 1 nm; convergence semi-angle, 19 mrad. Energy-Dispersive X-Ray spectroscopy (EDX) compositional maps were composed by registering Ti-K, Ru-L and Ce-L signals. Average Ruthenium cluster sizes were measured from the HAADF images by using ImageJ software, and the interpretation of atomic resolution images was assisted by Eje-Z software [20]. Atomic models for TEM/STEM image simulations were built using Rhodius software [21], which allows a total control of the orientation, the morphology, and the atomic positions of the nanostructures. This software is freely available online on the TEMserver web.

Additional details about other characterization techniques, such as X-ray diffraction and X-ray photoelectron spectroscopy are included in Supporting Information S1.

2.3 Photo-thermo catalytic tests

The photo-thermo formic acid decomposition catalytic tests were carried with a HCOOH concentration of 4600 ppm_v and using Ar as carrier gas at 14.7 mL/min The continuous-flow photo-thermo reactor consisted in a Harrick Scientific HVC-MRA 5 reaction chamber made from SS-316 alloy. 1.8 mg of the catalyst was homogeneously deposited as a thin layer at the surface density of 6 mg/cm^2 on a stainless meshed grid allowing the catalyst and the reactor to operate in a flow-through mode, with a formic acid specific molar rate of 67.2 $mmol \cdot g^{-1} \cdot h^{-1}$. The catalyst was homogeneously heated using an external cartridge heater monitored by a K-type thermocouple (±1°C), and using a high flow rate water cooling system for maintaining a constant (bulk) temperature. The catalyst was irradiated via a quartz window using a Thorlab M365LP1 LED (λ = 365 nm) with tunable and calibrated irradiance within the 0-365 mW/cm^2 range, and mounted on a lens to collimate the LED beam to the catalyst surface area. The irradiance was measured at 365 nm at the position of the photocatalyst. Prior to any experiment, oxygen was removed by Ar flushing. Further information about the photocatalytic experiments is gathered in Supporting Information S1.

The activity of the catalyst was expressed in terms of HCOOH conversion, H_2 selectivity, as well as of H_2, CO_2 and CO production in $mmol \cdot g^{-1} \cdot h^{-1}$, calculated as follows:

$$HCOOH\ conversion\ (\%) = \frac{[H_2]+[CO]}{[HCOOH]_{in}}\ x\ 100 \quad (3)$$

$$H_2\ selectivity\ (\%) = \frac{[H_2]}{[H_2]+[CO]}\ x\ 100 \quad (4)$$

The carbon balance was verified as follows:

$$C\ balance\ (\%) = \frac{[CO_2]+[CO]+[HCOOH]_{out}}{[HCOOH]_{in}}\ x\ 100 \quad (5)$$

$[HCOOH]_{in}$ and $[HCOOH]_{out}$ are the inlet and outlet HCOOH concentrations, respectively. H_2 and CO_2 can be used independently for calculating the HCOOH conversion

and the H_2 selectivity, as they are formed in an equimolar ratio in agreement with the dehydrogenation route. The carbon balance was calculated within the 98-102% range for all the photo-thermo catalytic tests.

Complementary tests targeting the 4-chlorophenol photocatalytic degradation is described in Supporting Information S1.

3. Results and discussion

3.1 Support characterization

The XRD patterns of the TiO_2 and ceria-modified TiO_2 supports are shown in Supporting Information S2. They confirmed the presence of both anatase and rutile TiO_2 crystallographic phases, with an anatase/rutile ratio around 85/15, while no fluorite peaks corresponding to the lanthanide-based phase were observed, suggesting a high dispersion for the supported CeO_2. ICP-AES chemical analysis confirmed the presence of cerium in the support with a CeO_2 content of 2.0 wt.%. Additionally, the Ce oxidation state was determined from XPS experiments, evaluating the binding energy of the Ce 3d core orbitals to figure out the Ce^{3+} and Ce^{4+} components, as shown in Supporting Information S3. Special care was taken on using a low exposure time, achieved by applying a high pass energy in order to avoid the CeO_2 reduction during the acquisition. The calculated fraction of reduced Ce atoms at the surface is 58%.

The nature of the cerium-based supported phase and its spatial distribution on TiO_2 were revealed by electron microscopy, together with the nature of the interface with TiO_2. First, HAADF-STEM images show representative CeO_2 nanoparticles highly dispersed on the TiO_2 surface (Fig. 1A and B), revealing their flat morphology, with an average width of 4.3 ± 1.3 nm, an average height of 1.8 ± 0.5 nm and a narrow distribution. High resolution TEM in combination with image simulations shown in Fig. 1C-E, has unveiled an epitaxial growth between {002} fluorite and {112} anatase planes, respectively on the [010] and [-111] zone axis, what allows to propose a favored location of CeO_2 at the edges of TiO_2 nanoparticles. The {112} facets with restricted size given their higher surface energy, are indeed described as a chamfer between low-index {101} planes in a typical pseudo-octahedral model of an anatase nanoparticle. This structural match between the two phases was already reported in [22].

Besides the epitaxy, a high interaction energy between the CeO_2-{002} and TiO_2-{112} planes may explain the flattened morphology of the ceria phase.

Moreover, HAADF images evidenced that Ce exists not only in the form of flat epitaxied CeO_2 nanoparticles, but also as CeO_x nanoclusters highly dispersed at the TiO_2 surface, as indicated by the yellow circle in Fig. 1A. This population of highly dispersed lanthanide is better observed from a profile view (Fig. 1G), where the titania nanoparticle is decorated with bright spots corresponding to CeO_x. This phenomenon is analytically confirmed by means of a combination of HAADF and EDX (Supporting Information S4), demonstrating that the brightness of the surface corresponds to a Ce enrichment. Similar ultra-dispersed Ce-based species have been previously detected on a TiO_2 (110) surface by Park et al. using Scanning Tunneling Microscopy [23], and assigned to CeO_x clusters (mainly dimers) with Ce in +3 oxidation state as evidenced by XPS measurements.

3.2 Synthesis monitoring and catalyst characterization

Supporting Information S5 illustrates the monitoring of the photon-assisted synthesis of both Ru catalysts by showing the evolution of the relative concentration of the Ru precursor. First, no photolysis occurred under UV-A light in the absence of TiO_2. After the initial adsorption period in the dark, complete disappearance of the Ru precursor was observed upon illumination of the support suspension for a reaction time of 60 min and 120 min in the case of CeO_2/TiO_2 and TiO_2, respectively. Ruthenium contents of 0.40 wt% and 0.44 wt% were determined by ICP-AES for TiO_2 and CeO_2/TiO_2, respectively, in agreement with the targeted nominal value of 0.5 wt.%.

Fig. 2A shows a representative HAADF image of the Ru/TiO_2 sample and reveals the highly dispersed nature of the Ru species, with bright spots distributed over the support surface that correspond to small clusters and even single atoms. The size distribution shown in Fig. 2B has been built using a tailored protocol to consider the presence of highly dispersed species [24]. The high dispersion of Ru species presents a mean diameter value of 0.36 nm, with no Ru entities being detected above 1 nm in size. To further characterize the Ru species observed experimentally, careful and compelling processing of HAADF images has been performed in combination with image simulations. Fig. 2C depicts an atomic model built to represent a Ru single atom supported on a (001) TiO_2 plane with a total thickness of 17 nm and slightly tilted to match the fringes observed in experimental images, and a zoom of the front view following the electrons trajectory is shown in Fig. 2D. The corresponding HAADF simulated image of Fig. 2E points out that the Ru single atom matches a size of around 0.15 nm, in agreement with the left size of our size distribution. Note that the cumulative frequency for the bin 0.1-0.15 nm, i.e. those corresponding to single atom species, is roughly 30%. If we also consider clusters with low atomicity (sizes below 0.3 nm), the accumulated frequency increases to about 60% of the total population, meaning that most of the Ru species exhibit a low coordination. Korobova et al. recently reported the stabilization of Ru as single atoms in addition to the presence of ultrafine Ru particles (<2 nm) on N-modified carbon nanotubes [8].

In the case of the $Ru/CeO_2/TiO_2$ catalyst, the surface modification of the TiO_2 support did not alter the efficiency of the photon-assisted synthesis method. The bright dots observed at the TiO_2 surface in the HAADF images of Fig. 3A and B indicated the presence of both nanoclusters and single atoms species. However, given the aforementioned characterization of both the CeO_2/TiO_2 support and the Ru/TiO_2 catalyst, a more complex nature is expected for the $Ru/CeO_2/TiO_2$ catalyst, as low atomicity species corresponding to both metallic and lanthanide phases may coexist at the TiO_2 surface. The HAADF image and its corresponding

EDX map (Fig. 3C and D) showed a representative CeO_2 nanoparticle decorated by a Ru cluster, the deposition of metallic phase on the ceria nanoparticle being materialized by the intense Ru peak in the EDX spectrum extracted from this region (Fig. 3E, spectrum 1). The presence of low atomicity entities was visualized by bright spots in the HAADF image, with minor peaks in the EDX spectrum corresponding to Ru and Ce phases (Fig. 3E, spectrum 2, black arrows). The observation demonstrates the high dispersion of Ru clusters, either directly interfaced with CeO_2 nanoparticles or distributed over the bare TiO_2 surface in close vicinity with the low atomicity CeO_x species.

The Ru oxidation state was confirmed by analyzing the Ru 3d primary region XPS spectra for both Ru-based catalysts (Supporting Information S6). Both Ru^0 and Ru^{4+} species were observed, in agreement with our previous studies on the elaboration of Ru/TiO_2 catalysts through the photon-assisted synthesis method [6,14,25]. The presence of two Ru 3d5/2-Ru3d3/2 orbital doublet contributions at 280.4 eV and 282.1 eV, respectively, with a 4.1 eV spin orbit splitting constant, was evidenced in addition to the contributions due to the adventitious C 1s carbon that complexifies the analysis of the multi-contribution envelope for Ru/TiO_2 systems [26–28]. Considering the ultra-dispersion of the Ru clusters and single atoms, oxidation of the metal by exposure to the air is expected.

3.3 Photo-thermo catalytic activity of the catalysts

3.3.1 Dehydration activity of the supports

The influence of the UV-A irradiance and the reaction temperature on the catalytic activity of both TiO_2 and CeO_2/TiO_2 supports in the decomposition of gaseous HCOOH is shown in Fig. 4. Both supports catalyzed selectively the dehydration of HCOOH into CO,

neither CO_2 nor H_2 dehydrogenation products being detected, regardless of whether the reaction is carried out under irradiation or in the dark. The CO production rate increases with the increase in the reaction temperature, e.g. reaching 0.4 mmol/g·h and 7.0 mmol/g·h at 130°C and 170°C, respectively, and is boosted upon irradiation to reach 27.1 mmol/g·h and 46.1 mmol/g·h at 365 mW/cm^2 at the same temperatures, as previously observed in Ivanez et al. [8]. Most of the transition oxides are reported to decompose HCOOH, through the formation of a formate adsorbate and the donation of a proton to the catalyst while TiO_2-P25 was reported to form selectively CO [29,30]. A reaction mechanism involving lattice oxygens and the formation of oxygen vacancies was proposed by Henderson [31]:

$$2\,HCOOH + 2\,O^{2-}_{lattice} \rightarrow 2\,HCOO^{-}_{ad} + 2\,OH^{-}_{lattice} \quad (6)$$

$$2\,OH^{-}_{lattice} \rightarrow H_2O + O^{2-}_{lattice} + vac \quad (7)$$

$$2\,HCOO^{-}_{ad} \rightarrow 2\,CO + 2\,OH^{-}_{ad} \quad (8)$$

$$2\,OH^{-}_{ad} \rightarrow H_2O + O^{2-}_{ad} \quad (9)$$

$$O^{2-}_{ad} + vac \rightarrow O^{2-}_{lattice} \quad (10)$$

Through kinetics and isotopic methods as well as DFT analysis of the different transition steps in the HCOOH decomposition, Kwon et al. considered recently the role of Ti-O site pairs consisting in two-coordinate O (O_{2c}) and five-coordinate Ti (Ti_{5c}) on the titania surface [32].

Interestingly, the addition of CeO_2 triggers a strong lowering of the CO production rate in the dark, and only 1.3 mmol/g·h was formed at 170ºC, *vs.* 7.0 mmol/g·h with bare TiO_2. The partial coverage of TiO_2 by ceria, either in the form of nanoparticles or small clusters, could potentially block some of the TiO_2 surface active sites and may contribute to reducing the

HCOOH dehydration into CO. However, given the relatively low ceria amount at *ca.* a quarter of a theoretical monolayer and the degree of coverage observed in HAADF images (Fig. 1), it could also be proposed that ceria-induced electronic effects at the TiO_2 surface altered the adsorption of HCOOH. The presence of Ce mainly as reduced phase at the interface with TiO_2 might be indicative of a high fraction of oxygen vacancies, that could favor a too strong HCOOH adsorption at the CeO_2/TiO_2 interface, and thus hinder the subsequent decomposition of the molecule [33,34]. Indeed, adsorption energies for formic acid were calculated to be lower on reduced ceria (*ie.* containing oxygen vacancies) than on TiO_2 anatase.

Upon UV-A light irradiation, both HCOOH conversion and CO production were enhanced on bare TiO_2 and CeO_2/TiO_2 supports, the improvement being all the more marked as the irradiance was increasing. However, whatever the irradiance, the presence of CeO_2 allowed lower CO production to be achieved in comparison to the bare TiO_2, *eg.* 14.3 mmol/g·h at 170°C at 365 mW/cm^2 vs. 46.1 mmol/g·h. The mechanism underlying the promotion of the dehydration reaction upon irradiation of the oxide supports remains under investigation, and may imply a possible change of the surface chemistry or involve photogenerated charge carriers. Oxygen vacancies being involved in the dehydration mechanism proposed by Henderson, their light-induced generation that occurs together with the local reduction of Ti^{4+} to Ti^{3+} in TiO_2 upon irradiation might contribute to the enhancement under UV-A light of the CO production by HCOOH dehydration [35]. A higher mobility of the lattice oxygen in irradiated TiO_2 might also be hypothesized as being beneficial for the reaction. Also, the role of oxygenated radicals formed at the surface of the irradiated TiO_2 could be put forward, as they could boost the necessary reoxidation of the oxygen vacancies at the surface of the reducible oxide, and in consequence faster the HCOOH dehydration. A similar explanation was recently pointed out for describing the beneficial photo-thermo synergy during the

oxidation of a span of volatile organic compounds, that allowed the reaction to be driven at lower temperatures following a light-enhanced Mars-van-Krevelen mechanism [36–38].

In an effort to understand the role of promoter of CeO_2 under UV-A light, the photocatalytic degradation of the 4-chlorophenol probe molecule in water has been performed using both TiO_2 and CeO_2/TiO_2 samples (Supporting Information S7). While complete degradation of 4-chlorophenol was obtained on the TiO_2 reference within 60 min with a 1st-order apparent kinetic rate constant of 2.4 h^{-1} in agreement with the literature [39,40], it is worth noting that almost no activity was observed with the CeO_2/TiO_2 catalyst, giving a strongly reduced rate constant of $4.8 \cdot 10^{-2}$ h^{-1}. Given the more cathodic potential of the valence band of ceria, this behavior could result from the transfer of the photogenerated holes from the valence band of TiO_2 to that of ceria, according to the semiconductor heterojunction scheme and the respective position of their electronic bands [41]. The trapping of the photogenerated holes in ceria might also be favored by the important fraction of easily oxidizable Ce^{3+} species and its associated oxygen vacancies at the surface of TiO_2. Also, the heterojunction nature of the CeO_2/TiO_2 system with hole transfer to ceria is expected to extend the lifetime of the photogenerated electrons necessary for the reduction of the Ru precursors adsorbed at the semiconductor surface into metallic Ru, what correlates well with the faster reduction observed in Supporting Information S5.

3.3.2 Activity of the Ru-based catalysts

Fig. 5 shows the influence of the irradiance and the reaction temperature on the performances obtained with Ru/TiO_2 and $Ru/CeO_2/TiO_2$ catalysts. By contrast to the pure supports, the Ru-based catalysts drive the decomposition of HCOOH through both dehydration and dehydrogenation pathways, leading to the production of CO and H_2 regardless of the irradiance and the reaction temperature. CO_2 and H_2 were formed with an equimolar ratio

whatever the reaction conditions, what means that the main side reactions forming methane or formaldehyde were negligible in our conditions (Eqs. 11-13) [28]:

$$CO + 3\,H_2 \rightarrow CH_4 + H_2O \quad (11)$$

$$CO_2 + 4\,H_2 \rightarrow CH_4 + 2\,H_2O \quad (12)$$

$$2\,HCOOH \rightarrow HCHO + CO_2 + H_2O \quad (13)$$

In terms of H_2 production, the presence of CeO_2 barely alters the H_2 production, both Ru/TiO_2 and $Ru/CeO_2/TiO_2$ catalysts being characterized by relatively similar performances in the dark independently of the reaction temperature. The addition of CeO_2 is mainly blocking the dehydration route at the surface of TiO_2 but not modifying the dehydrogenation performance taking place on the Ru species, allowing thus the improvement of the selectivity towards H_2 (*eg.* at 170°C from 48% to 77% when adding ceria).

With additional photonic excitation, the H_2 production was strongly enhanced to similar extents on both catalysts regardless of the presence of ceria, *eg.* at 150°C from *ca.* 2.3 mmol/g·h in the dark to 9.2 mmol/g·h and 32.4 mmol/g·h at 126 mW/cm^2 and 365 mW/cm^2, respectively. By contrast, the $Ru/CeO_2/TiO_2$ catalyst lowered the CO production compared to its Ru/TiO_2 counterpart. This positively affected the selectivity towards H_2, *eg.* with an increase from 62% to 75% (at 130°C and 365 mW/cm^2) or from 53% to 65% (at 150°C and 126 mW/cm^2) when adding ceria. However, Ru in intimate contact with the CeO_2 support has been reported to favor the presence of oxygen vacancies [42,43], that might also contribute to the production of CO by HCOOH dehydration, and explain its photonic enhancement. In consequence, the gain in H_2 selectivity on the $Ru/CeO_2/TiO_2$ catalyst *vs.* the Ru/TiO_2 reference is less pronounced in a dual excitation mode than in dark conditions.

On both $Ru/CeO_2/TiO_2$ and Ru/TiO_2 catalysts, conducting the catalytic HCOOH decomposition under combined photonic/thermal excitation reduced the apparent activation energy for both dehydration and dehydrogenation reactions (Fig. 6 A-F). The apparent activation energy for the dehydrogenation to H_2 decreased from 87.4 kJ/mol ($Ru/CeO_2/TiO_2$) and 103.1 kJ/mol (Ru/TiO_2) in the dark, down to 34.7 kJ/mol and 35.4 kJ/mol, respectively, at 365 mW/cm^2. The synergy observed under combined photonic/thermal excitation allowed to drive the reaction at a lower temperature while keeping similar levels of H_2 production compared to the performances in the dark. For instance, on $Ru/CeO_2/TiO_2$, a low-temperature shift of 80°C was obtained under 365 mW/cm^2 with *ca.* 20.5 mmol/g·h of H_2 being produced at 110°C *vs.* at 190°C in the dark, while keeping similar levels of CO production at *ca.* 6.5 mmol/g·h.

The lowering of the apparent activation energy upon irradiation does not usually characterize a mechanism of localized heat supply through a light-to-heat conversion process with dissipative non-radiative relaxation. Indeed, Ru is not considered to act as plasmonic metal in comparison to more popular Au, Ag or Cu [44]. However, Ru is reported to show significant UV and visible light absorption, *via* an electronic mechanism involving interband transitions of bounded electrons [45–47], and the conversion of molecules adsorbed on the surface of non-plasmonic metal nanoparticles has already been suggested to occur through the participation of light-excited electrons from the metal [48,49]. In consequence, the reduction of the apparent activation energy upon irradiation might be the fingerprint of a reaction mechanism involving the light-excited electrons from Ru with the establishment of an alternative low-energy transition state allowing the reaction kinetics to be controlled through a new dark-type rate-determining step [3].

To summarize, while TiO_2 and Ce-modified TiO_2 supports only display catalytic activity in the dehydration of formic acid into CO due to their surface properties, Ru provides dehydrogenating properties to the catalyst, regardless of whether the catalyst is irradiated or not. Under light, the excitation of the electrons from Ru is proposed to allow the thermal reaction kinetics to be controlled through a new dark-type rate-determining step, ie. via an electron-driven mechanism rather than a localized heat-delivery mechanism. Additionally, CeO_2 is proposed to induce electronic effects at the TiO_2 surface that block the dehydration route and lower the CO formation without modifying the dehydrogenation activity of the Ru species, allowing thus the improvement of the H_2 selectivity towards. Upon irradiation, it is favored the formation of oxygen vacancies and the mobility of lattice oxygen on TiO_2, while oxygenated radicals formed at the TiO_2 surface under light would boost the reoxidation of the oxygen vacancies and faster the formic acid dehydration into CO. The formation of the CeO_2/TiO_2 heterojunction is proposed to allow for the transfer of the photogenerated holes from TiO_2 to ceria, inhibiting partially the above mechanism. Besides the transfer of photogenerated holes from TiO_2 to ceria in the irradiated heterojunction, the role of the electrons and holes from TiO_2 still remains to clarify.

4. Conclusions

CeO_2/TiO_2 supported Ru photo-thermo catalysts were prepared according to a solar photon-assisted synthesis method using Ru chloride as precursor and TiO_2-P25 modified with ceria through incipient wetness impregnation at a quarter of the theoretical monolayer as host surface. Characterization by advanced electron microscopy techniques unraveled that the CeO_2/TiO_2 support exposes two well-defined ceria-based nanostructures, namely flat nanometric size CeO_2 nanoparticles epitaxied with a preferential distribution over {112} facets

of anatase, as well as highly-dispersed CeO_x clusters decorating the TiO_2 surface. Modifying TiO_2 with ceria did not alter the efficiency of the photon-assisted synthesis to achieve an homogeneous and ultra-dispersed Ru distribution over the support surface, and the $Ru/CeO_2/TiO_2$ catalyst was characterized by a well-distributed population of Ru nanoclusters, with a large fraction of low atomicity Ru species. In particular, image processing in combination with image simulations have allowed the identification of Ru single atoms. EDX analyses have demonstrated that the ultra-dispersed metallic Ru species could be directly interfaced in intimate contact with CeO_2 or distributed over the TiO_2 surface in close vicinity with low atomicity CeO_x species.

The catalytic studies bring to light that the homogeneous and partial coverage of the TiO_2 surface by cerium-based species strongly lowers the CO production rate in the dark that results from the detrimental intrinsic dehydration activity of the bare TiO_2 support itself. In consequence, the $Ru/CeO_2/TiO_2$ catalyst drives the decomposition of formic acid more selectively towards H_2 production by dehydrogenation in comparison to the Ru/TiO_2 reference. Performing the reaction under a dual photonic/thermal excitation boosted further the decomposition of gaseous formic acid to H_2 compared to dark conditions, the increase in conversion and H_2 production rate being all the more marked as the irradiance was high. Consequently, we evidenced that the combined excitation enables the dehydrogenation reaction to be driven with a similar H_2 production rate under milder conditions compared to the dark conditions, *ie.* with a low-temperature shift of *ca.* 80ºC under light while 190°C is required in dark conditions. However, albeit observed, the gain in H_2 selectivity on the $Ru/CeO_2/TiO_2$ catalyst was less pronounced in a dual excitation mode than in dark conditions.

Author Contributions

The manuscript was written through the contributions of all authors. All authors have given approval to the final version of the manuscript.

CRediT author statement

José M. Montes-Monroy: Methodology, Investigation, Formal analysis.

Ramón Manzorro: Methodology, Investigation, Formal analysis, Software, Writing - original draft.

Laura Valenzuela Ávila: Investigation.

Javier Ivanez: Investigation.

José A. Pérez-Omil: Conceptualization, Supervision, Funding acquisition, Project administration, Resources.

Nicolas Keller: Conceptualization, Funding acquisition, Investigation, Formal analysis, Writing – original draft, Project administration, Supervision, Resources.

Declaration of Competing Interest

The authors declare no competing financial interest.

Data availability

Data will be made available on request.

Acknowledgement

The IdEx Program of the University of Strasbourg is acknowledged for funding the PhD fellowship of J. Ivanez. The MOPGA program is acknowledged for funding the fellowship of L. Valenzuela. V. Papaefthimiou (ICPEES) is thanked for the XPS characterization. This work has also received funding from National Projects PID2020-113006-RB-I00 and PID2022-142312NB-I00 funded by MCIN/AEI/10.13039/501100011033 and by "ERDF- A way of making Europe". R. Manzorro gratefully acknowledges financial support from Cádiz University (Young Researchers, Project PR2022-046). Electron microscopy studies were performed at the DME-UCA node of the Spanish Unique Infrastructure (ICTS) on Electron Microscopy of Materials ELECMI.

Figures and captions

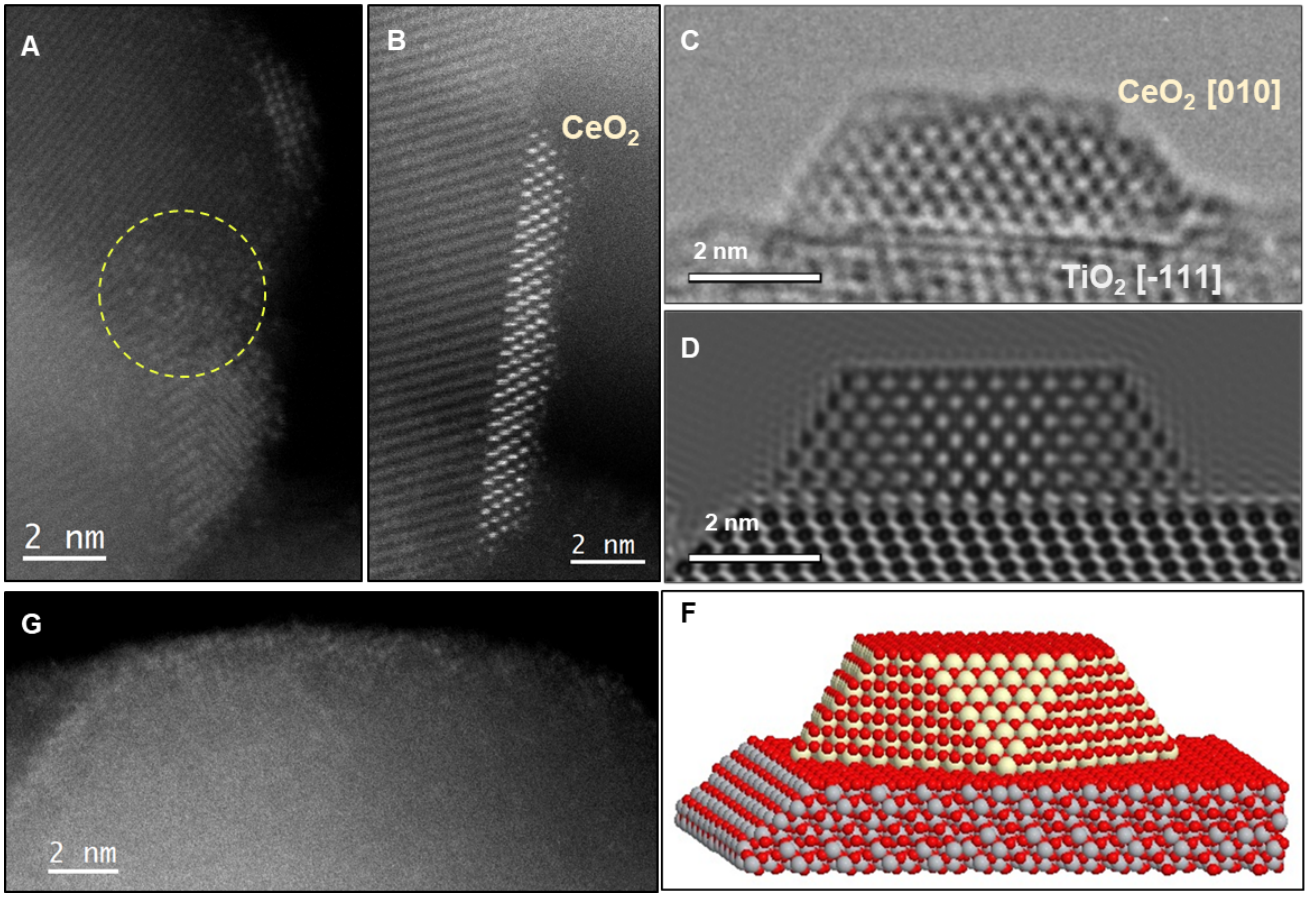

Fig. 1. CeO_2/TiO_2 support electron microscopy characterization. A, B) HAADF representative images illustrating the dispersion of CeO_2 flattened nanoparticles on top of TiO_2 particles. C, D, F) Experimental HRTEM image together with the atomic model and the simulated image confirming the structural match between the CeO_2-(200) and TiO_2-(112) crystallographic planes. G) HAADF image showing the profile view of TiO_2 surface with CeO_x enrichment.

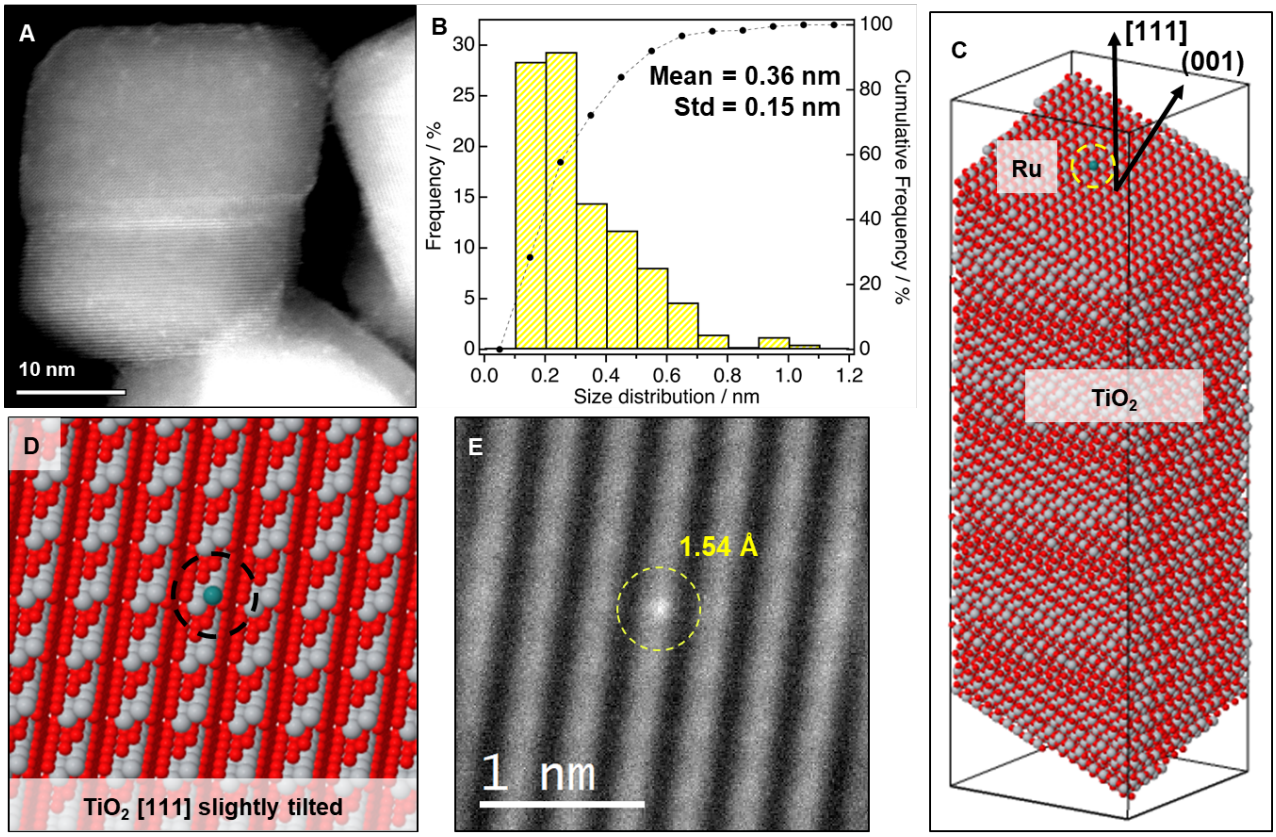

Fig. 2. Distribution of Ru nanoclusters. A) HAADF corresponding to the Ru/TiO_2 sample. B) Ru particle/cluster size distribution. C, D). Atomic models corresponding to a supported Ru single atoms on top of a (001) TiO_2 plane. E) HAADF simulated image of this atomic model confirming the sizes observed experimentally.

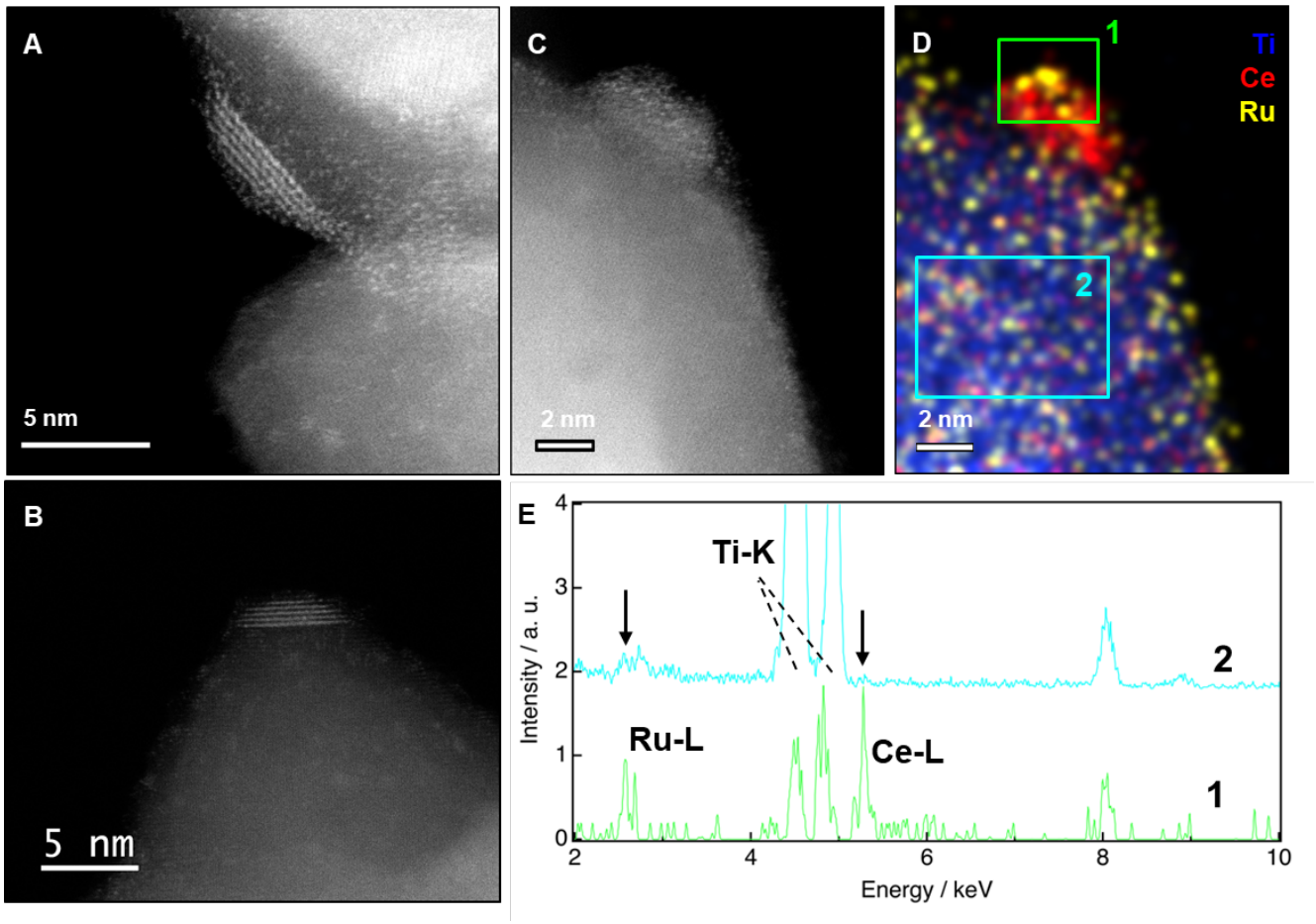

Fig. 3. Characterization of the $Ru/CeO_2/TiO_2$ catalyst. A, B) Representative HAADF images corresponding to the ceria-modified Ru/TiO_2 catalyst. C, D). Combination of HAADF with its EDX map displaying the Ti, Ce and Ru elemental distribution in blue, red and yellow colors, respectively. E) EDX spectra extracted from the regions depicted by boxes 1 and 2.

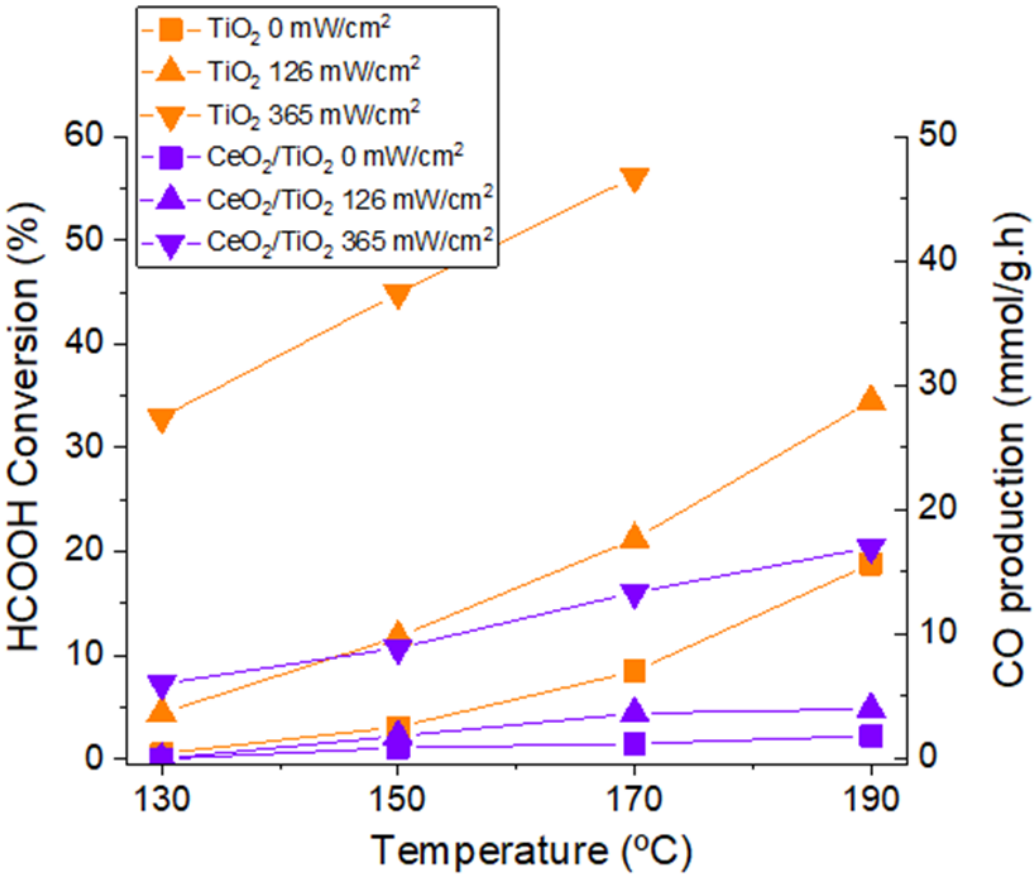

Fig. 4. Influence of the UV-A irradiance and the reaction temperature on the catalytic activity of the bare TiO_2 and CeO_2/TiO_2 supports in the gas phase HCOOH decomposition.

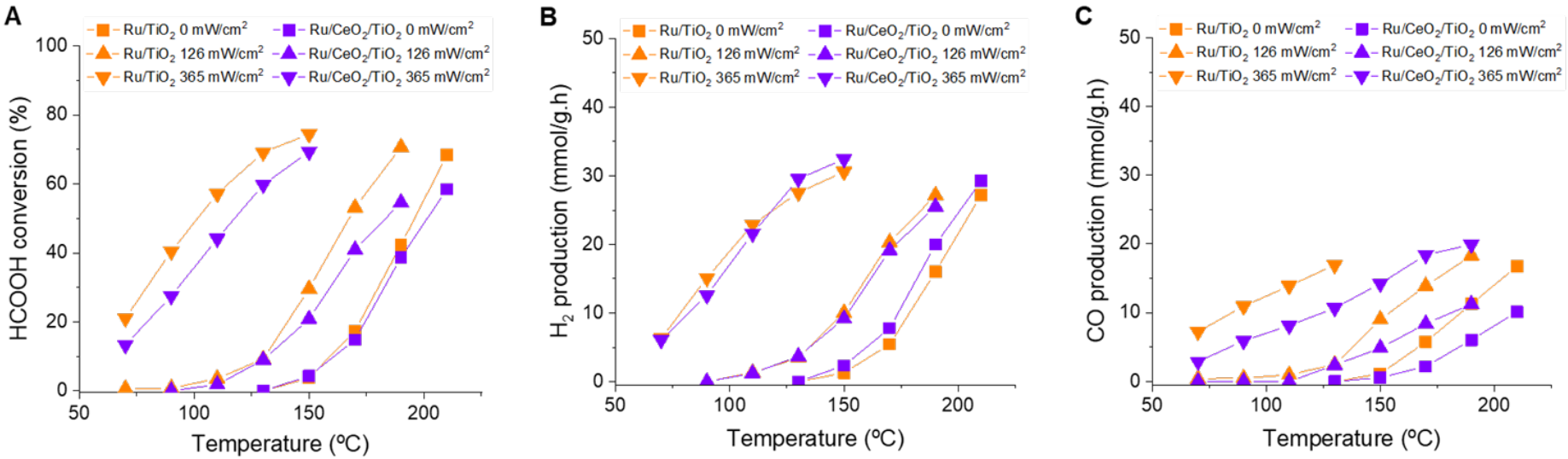

Fig. 5. Influence of the UV-A irradiance and the reaction temperature on the catalytic activity of the Ru/TiO_2 and $Ru/CeO_2/TiO_2$ catalysts in the gas phase HCOOH decomposition. CO_2 production is not reported as being exactly equimolar to the H_2 production. The performances of the catalysts in some specific temperature/irradiance conditions are not reported due to too high or low HCOOH conversions.

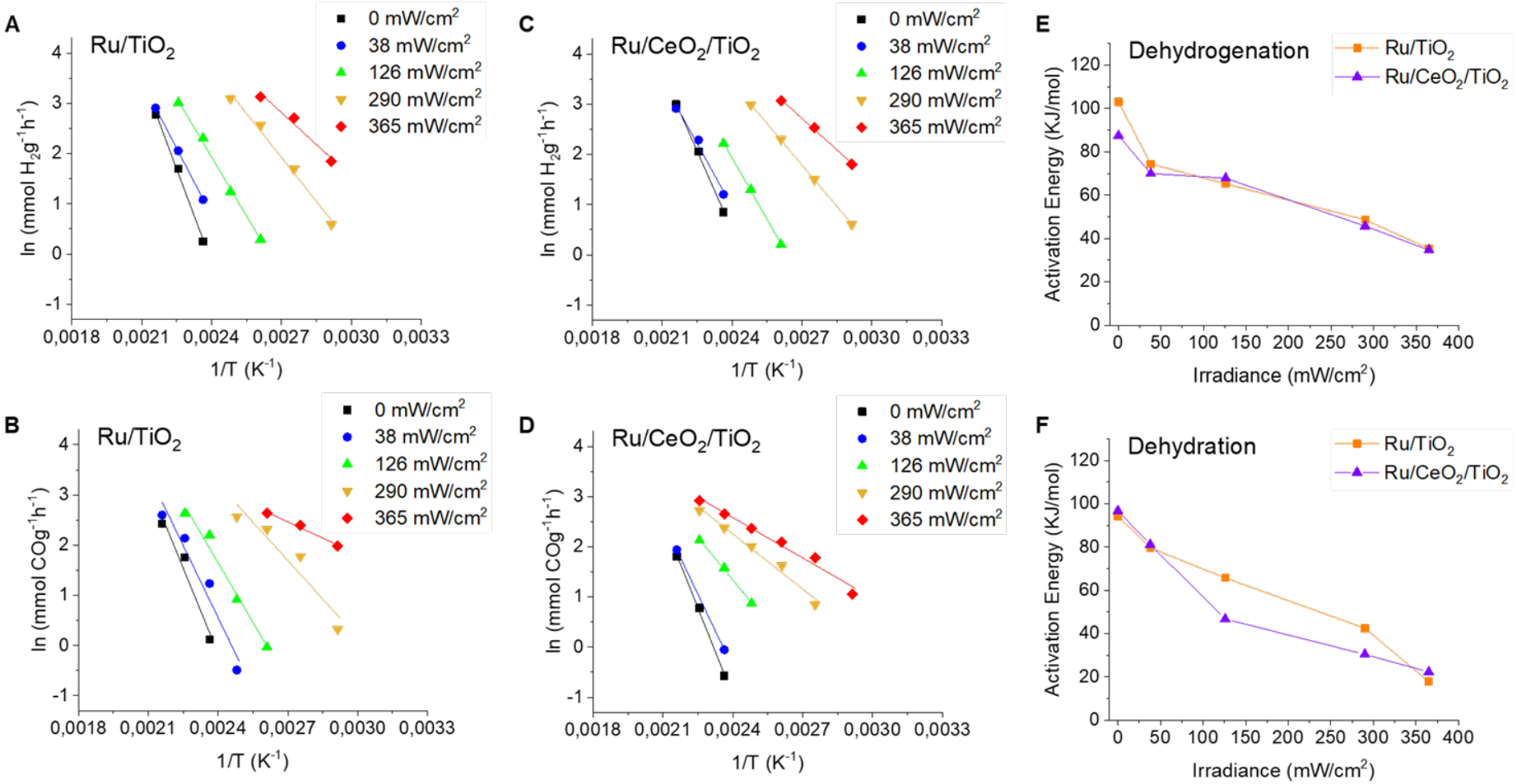

Fig. 6. Arrhenius plots for the dark and light-induced reactions with Ru/TiO_2 and $Ru/CeO_2/TiO_2$ catalysts and influence of the UV-A irradiance on the apparent activation energy for (A, C, E) H_2 and (B, D, F) CO productions.

References

[1] A. Iglesias-Juez, F. Fresno, J.M. Coronado, J. Highfield, A.M. Ruppert, N. Keller, Emerging high-prospect applications in photothermal catalysis, Curr. Opin. Green Sustain. Chem. 37 (2022) 100652. https://doi.org/10.1016/j.cogsc.2022.100652.

[2] D. Mateo, J.L. Cerrillo, S. Durini, J. Gascon, Fundamentals and applications of photo-thermal catalysis, Chem. Soc. Rev. 50 (2021) 2173–2210. https://doi.org/10.1039/D0CS00357C.

[3] N. Keller, J. Ivanez, J. Highfield, A.M. Ruppert, Photo-/thermal synergies in heterogeneous catalysis: Towards low-temperature (solar-driven) processing for sustainable energy and chemicals, Appl. Catal. B. 296 (2021) 120320. https://doi.org/10.1016/j.apcatb.2021.120320.

[4] Z. Wang, H. Song, H. Liu, J. Ye, Coupling of Solar Energy and Thermal Energy for Carbon Dioxide Reduction: Status and Prospects, Angew. Chem. Int. Ed. 59 (2020) 8016–8035. https://doi.org/10.1002/anie.201907443.

[5] C. Song, Z. Wang, Z. Yin, D. Xiao, D. Ma, Principles and applications of photothermal catalysis, Chem Catal. 2 (2022) 52–83. https://doi.org/10.1016/j.checat.2021.10.005.

[6] J. Ivanez, P. Garcia-Munoz, A.M. Ruppert, N. Keller, UV-A light-assisted gas-phase formic acid decomposition on photo-thermo Ru/TiO_2 catalyst, Catal. Today 380 (2021) 138–146. https://doi.org/10.1016/j.cattod.2021.03.020.

[7] M. Zacharska, O.Yu. Podyacheva, L.S. Kibis, A.I. Boronin, B.V. Senkovskiy, E.Yu. Gerasimov, O.P. Taran, A.B. Ayusheev, V.N. Parmon, J.J. Leahy, D.A. Bulushev, Ruthenium Clusters on Carbon Nanofibers for Formic Acid Decomposition: Effect of Doping the Support with Nitrogen, ChemCatChem 7 (2015) 2910–2917. https://doi.org/10.1002/cctc.201500216.

[8] A. Korobova, N. Gromov, T. Medvedeva, A. Lisitsyn, L. Kibis, O. Stonkus, V. Sobolev, O. Podyacheva, Ru Catalysts Supported on Bamboo-like N-Doped Carbon Nanotubes: Activity and Stability in Oxidizing and Reducing Environment, Materials 16 (2023). https://doi.org/10.3390/ma16041465.

[9] Y. Wu, M. Wen, M. Navlani-García, Y. Kuwahara, K. Mori, H. Yamashita, Palladium Nanoparticles Supported on Titanium-Doped Graphitic Carbon Nitride for Formic Acid Dehydrogenation, Chem. Asian J. 12 (2017) 860–867. https://doi.org/10.1002/asia.201700041.

[10] Y.-Y. Cai, X.-H. Li, Y.-N. Zhang, X. Wei, K.-X. Wang, J.-S. Chen, Highly Efficient Dehydrogenation of Formic Acid over a Palladium-Nanoparticle-Based Mott–Schottky Photocatalyst, Angew. Chem. Int. Ed. 52 (2013) 11822–11825. https://doi.org/10.1002/anie.201304652.

[11] X. Wang, Q. Meng, L. Gao, Z. Jin, J. Ge, C. Liu, W. Xing, Recent progress in hydrogen production from formic acid decomposition, Int. J. Hydrogen Energy. 43 (2018) 7055–7071. https://doi.org/10.1016/j.ijhydene.2018.02.146.

[12] D.A. Bulushev, L.G. Bulusheva, Catalysts with single metal atoms for the hydrogen production from formic acid, Catal. Rev. Sci. Eng. 64 (2022) 835–874. https://doi.org/10.1080/01614940.2020.1864860.

[13] A.M. Ruppert, M. Jędrzejczyk, N. Potrzebowska, K. Kaźmierczak, M. Brzezińska, O. Sneka-Płatek, P. Sautet, N. Keller, C. Michel, J. Grams, Supported gold–nickel nano-alloy as a highly efficient catalyst in levulinic acid hydrogenation with formic acid as an internal hydrogen source, Catal. Sci. Technol. 8 (2018) 4318–4331. https://doi.org/10.1039/C8CY00462E.

[14] J. Wojciechowska, M. Jędrzejczyk, J. Grams, N. Keller, A.M. Ruppert, Enhanced Production of γ-Valerolactone with an Internal Source of Hydrogen on Ca-Modified TiO_2 Supported Ru Catalysts, ChemSusChem 12 (2019) 639–650. https://doi.org/10.1002/cssc.201801974.
[15] F. Valentini, V. Kozell, C. Petrucci, A. Marrocchi, Y. Gu, D. Gelman, L. Vaccaro, Formic acid, a biomass-derived source of energy and hydrogen for biomass upgrading, Energy Environ. Sci. 12 (2019) 2646–2664. https://doi.org/10.1039/C9EE01747J.
[16] J. Eppinger, K.-W. Huang, Formic Acid as a Hydrogen Energy Carrier, ACS Energy Lett. 2 (2017) 188–195. https://doi.org/10.1021/acsenergylett.6b00574.
[17] T. Bunluesin, R.J. Gorte, G.W. Graham, Studies of the water-gas-shift reaction on ceria-supported Pt, Pd, and Rh: Implications for oxygen-storage properties, Appl. Catal. B. 15 (1998) 107–114. https://doi.org/10.1016/S0926-3373(97)00040-4.
[18] Y. Li, M. Kottwitz, J.L. Vincent, M.J. Enright, Z. Liu, L. Zhang, J. Huang, S.D. Senanayake, W.-C.D. Yang, P.A. Crozier, R.G. Nuzzo, A.I. Frenkel, Dynamic structure of active sites in ceria-supported Pt catalysts for the water gas shift reaction, Nat. Commun. 12 (2021) 914. https://doi.org/10.1038/s41467-021-21132-4.
[19] R. Manzorro, J.M. Montes-Monroy, D. Goma-Jiménez, J.J. Calvino, J.A. Pérez-Omil, S. Trasobares, Improving the reducibility of CeO_2/TiO_2 by high-temperature redox treatment: the key role of atomically thin CeO_2 surface layers, J. Mater. Chem. A 10 (2022) 13074–13087. https://doi.org/10.1039/D1TA08348A.
[20] S. Bernal, F.J. Botana, J.J. Calvino, C. López, J.A. Pérez-Omil, J.M. Rodríguez-Izquierdo, High-resolution electron microscopy investigation of metal–support interactions in Rh/TiO_2, J. Chem. Soc., Faraday Trans. 92 (1996) 2799–2809. https://doi.org/10.1039/FT9969202799.
[21] S. Bernal, F.J. Botana, J.J. Calvino, C. López-Cartes, J.A. Pérez-Omil, J.M. Rodríguez-Izquierdo, The interpretation of HREM images of supported metal catalysts using image simulation: profile view images, Ultramicroscopy 72 (1998) 135–164. https://doi.org/10.1016/S0304-3991(98)00009-6.
[22] A.C. Johnston-Peck, S.D. Senanayake, J.J. Plata, S. Kundu, W. Xu, L. Barrio, J. Graciani, J.Fdez. Sanz, R.M. Navarro, J.L.G. Fierro, E.A. Stach, J.A. Rodriguez, Nature of the Mixed-Oxide Interface in Ceria–Titania Catalysts: Clusters, Chains, and Nanoparticles, J. Phys. Chem. C 117 (2013) 14463–14471. https://doi.org/10.1021/jp3125268.
[23] J.B. Park, J. Graciani, J. Evans, D. Stacchiola, S.D. Senanayake, L. Barrio, P. Liu, J.Fdez. Sanz, J. Hrbek, J.A. Rodriguez, Gold, Copper, and Platinum Nanoparticles Dispersed on $CeO_x/TiO_2(110)$ Surfaces: High Water-Gas Shift Activity and the Nature of the Mixed-Metal Oxide at the Nanometer Level, J. Am. Chem. Soc. 132 (2010) 356–363. https://doi.org/10.1021/ja9087677.
[24] J.J. Calvino, M. López-Haro, J.M. Muñoz-Ocaña, J. Puerto, A.M. Rodríguez-Chía, Segmentation of scanning-transmission electron microscopy images using the ordered median problem, Eur. J. Oper. Res. 302 (2022) 671–687. https://doi.org/10.1016/j.ejor.2022.01.022.
[25] J. Wojciechowska, E. Gitzhofer, J. Grams, A.M. Ruppert, N. Keller, Light-driven synthesis of sub-nanometric metallic Ru catalysts on TiO_2, Catal. Today 326 (2019) 8–14. https://doi.org/10.1016/j.cattod.2018.07.013.
[26] J.C. Calderón, G. García, L. Calvillo, J.L. Rodríguez, M.J. Lázaro, E. Pastor, Electrochemical oxidation of CO and methanol on Pt–Ru catalysts supported on carbon nanofibers: the influence of synthesis method, Appl. Catal. B. 165 (2015) 676–686. https://doi.org/10.1016/j.apcatb.2014.10.077.

[27] M.-Y. Chen, Y.-B. Huang, H. Pang, X.-X. Liu, Y. Fu, Hydrodeoxygenation of lignin-derived phenols into alkanes over carbon nanotube supported Ru catalysts in biphasic systems, Green Chem. 17 (2015) 1710–1717. https://doi.org/10.1039/C4GC01992J.
[28] A.M. Ruppert, M. Jędrzejczyk, O. Sneka-Płatek, N. Keller, A.S. Dumon, C. Michel, P. Sautet, J. Grams, Ru catalysts for levulinic acid hydrogenation with formic acid as a hydrogen source, Green Chem. 18 (2016) 2014–2028. https://doi.org/10.1039/C5GC02200B.
[29] M. Ai, Activities for the decomposition of formic acid and the acid-base properties of metal oxide catalysts, J. Catal. 50 (1977) 291–300. https://doi.org/10.1016/0021-9517(77)90038-0.
[30] K.S. Kim, M.A. Barteau, Structural dependence of the selectivity of formic acid decomposition on faceted titania (001) surfaces, Langmuir 6 (1990) 1485–1488. https://doi.org/10.1021/la00099a009.
[31] M.A. Henderson, Complexity in the Decomposition of Formic Acid on the TiO_2(110) Surface, J. Phys. Chem. B 101 (1997) 221–229. https://doi.org/10.1021/jp961494i.
[32] S. Kwon, T.C. Lin, E. Iglesia, Formic Acid Dehydration Rates and Elementary Steps on Lewis Acid–Base Site Pairs at Anatase and Rutile TiO_2 Surfaces, J. Phys. Chem. C 124 (2020) 20161–20174. https://doi.org/10.1021/acs.jpcc.0c05721.
[33] Y. Wang, B. Wen, A. Dahal, G.A. Kimmel, R. Rousseau, A. Selloni, N.G. Petrik, Z. Dohnálek, Binding of Formic Acid on Anatase TiO_2(101), J. Phys. Chem. C 124 (2020) 20228–20239. https://doi.org/10.1021/acs.jpcc.0c06031.
[34] W.O. Gordon, Y. Xu, D.R. Mullins, S.H. Overbury, Temperature evolution of structure and bonding of formic acid and formate on fully oxidized and highly reduced CeO_2(111), Phys. Chem. Chem. Phys. 11 (2009) 11171–11183. https://doi.org/10.1039/B913310K.
[35] C. Xu, J.-L. Luo, Understanding the light-induced oxygen vacancy in the photochemical conversion, J. Phys. Energy 5 (2023) 011001. https://doi.org/10.1088/2515-7655/acb28f.
[36] R. Fiorenza, R.A. Farina, E.M. Malannata, F. Lo Presti, S.A. Balsamo, VOCs Photothermo-Catalytic Removal on MnO_x-ZrO_2 Catalysts, Catalysts 12 (2022). https://doi.org/10.3390/catal12010085.
[37] M. Bellardita, R. Fiorenza, L. D'Urso, L. Spitaleri, A. Gulino, G. Compagnini, S. Scirè, L. Palmisano, Exploring the Photothermo-Catalytic Performance of Brookite TiO_2-CeO_2 Composites, Catalysts 10 (2020). https://doi.org/10.3390/catal10070765.
[38] M. Mao, Y. Li, J. Hou, M. Zeng, X. Zhao, Extremely efficient full solar spectrum light driven thermocatalytic activity for the oxidation of VOCs on OMS-2 nanorod catalyst, Appl. Catal. B. 174–175 (2015) 496–503. https://doi.org/10.1016/j.apcatb.2015.03.044.
[39] B. Neppolian, H. Jung, H. Choi, Photocatalytic Degradation of 4-Chlorophenol Using TiO_2 and Pt-TiO_2 Nanoparticles Prepared by Sol-Gel Method, J. Adv. Oxid. Technol. 10 (2007) 369–374. https://doi.org/10.1515/jaots-2007-0222.
[40] P. Apopei, C. Catrinescu, C. Teodosiu, S. Royer, Mixed-phase TiO_2 photocatalysts: Crystalline phase isolation and reconstruction, characterization and photocatalytic activity in the oxidation of 4-chlorophenol from aqueous effluents, Appl. Catal. B. 160–161 (2014) 374–382. https://doi.org/10.1016/j.apcatb.2014.05.030.
[41] S.-W. Lin, M.-H. Tong, Y.-X. Chen, R. Chen, H.-P. Zhao, X. Jiang, K. Yang, C.-Z. Lu, CeO_2/TiO_2 Heterojunction Nanotube Arrays for Highly Efficient Visible-Light Photoelectrochemical Water Splitting, ACS Appl. Energy Mater. 6 (2023) 1093–1102. https://doi.org/10.1021/acsaem.2c03723.

[42] Z. Wang, Z. Huang, J.T. Brosnahan, S. Zhang, Y. Guo, Y. Guo, L. Wang, Y. Wang, W. Zhan, Ru/CeO_2 Catalyst with Optimized CeO_2 Support Morphology and Surface Facets for Propane Combustion, Environ. Sci. Technol. 53 (2019) 5349–5358. https://doi.org/10.1021/acs.est.9b01929.
[43] F. Wang, C. Li, X. Zhang, M. Wei, D.G. Evans, X. Duan, Catalytic behavior of supported Ru nanoparticles on the {100}, {110}, and {111} facet of CeO_2, J. Catal. 329 (2015) 177–186. https://doi.org/10.1016/j.jcat.2015.05.014.
[44] L. Yuan, B.B. Bourgeois, C.C. Carlin, F.H. da Jornada, J.A. Dionne, Sustainable chemistry with plasmonic photocatalysts, Nanophotonics 12 (2023) 2745–2762. https://doi.org/10.1515/nanoph-2023-0149.
[45] J.A. Creighton, D.G. Eadon, Ultraviolet–visible absorption spectra of the colloidal metallic elements, J. Chem. Soc., Faraday Trans. 87 (1991) 3881–3891. https://doi.org/10.1039/FT9918703881.
[46] T. Pakizeh, Optical absorption of nanoparticles described by an electronic local interband transition, J. Opt. 15 (2012) 025001. https://doi.org/10.1088/2040-8978/15/2/025001.
[47] J.H. Weaver, Optical properties of Rh, Pd, Ir, and Pt, Phys. Rev. B 11 (1975) 1416–1425. https://doi.org/10.1103/PhysRevB.11.1416.
[48] S. Sarina, H.-Y. Zhu, Q. Xiao, E. Jaatinen, J. Jia, Y. Huang, Z. Zheng, H. Wu, Viable Photocatalysts under Solar-Spectrum Irradiation: Nonplasmonic Metal Nanoparticles, Angew. Chem. Int. Ed. 53 (2014) 2935–2940. https://doi.org/10.1002/anie.201308145.
[49] S. Sarina, E.R. Waclawik, H. Zhu, Photocatalysis on supported gold and silver nanoparticles under ultraviolet and visible light irradiation, Green Chem. 15 (2013) 1814–1833. https://doi.org/10.1039/C3GC40450A.

Supporting information

H_2 production by formic acid decomposition on ceria-modified Ru/TiO_2 catalysts under dual photonic/thermal excitation

José M. Montes-Monroy,[a] Ramón Manzorro,[a] Laura Valenzuela Ávila,[b] Javier Ivanez,[b] José A. Pérez-Omil,[a] Nicolas Keller[b]

[a] Departamento de Ciencias de los Materiales e Ingeniería Metalúrgica y Química Inorgánica, Facultad de Ciencias, Universidad de Cádiz, Spain.

[b] Institut de Chimie et Procédés pour l'Energie, l'Environnement et la Santé (ICPEES), CNRS/Strasbourg University, 25 rue Becquerel, 67087 Strasbourg, France.

Supporting information S1: Experimental set-up details

X-ray Diffraction

X-ray diffraction (XRD) was performed to define the crystal structure of the samples by using an X-ray diffractometer D8 Advance A25 DAVINCI with radiation Cu Kα (λ = 1.5406 Å), step length 0.05º, step time 3s and experimental breadth 0.04º. Powder Cell software was used to estimate the phase composition and particle sizes for the supports. The specific surface areas were obtained by applying the BET method via N_2 physisorption at 77 K using an Micromeritics ASAP 2010 equipment from Quantachrome Instruments. Both CeO_2 and Ru final loadings were determined by ICP-AES and ICP-OES, respectively, after applying an adequate microwave-assisted acid digestion.

X-ray Photoelectron Spectroscopy

X-Ray Photoelectron Spectroscopy (XPS) characterization was performed on a ThermoVG Multilab ESCA 3000 spectrometer (Al Kα anode at hλ = 1486.6 eV). The energy shift due to electrostatic charging was adjusted using the C 1s band from the adventitious carbon, corrected at 284.8 eV. CasaXPS software was used for spectral processing.

Photo-thermo Catalytic Decomposition of Formic Acid

The final inlet flow was obtained by diluting a concentrated HCOOH/Ar flow with a pure Ar flow. To this end, an Ar flow (Air Liquide, ALPHAGAZ™ 1, ≥ 99,999 %) was bubbled at atmospheric pressure in a temperature-controlled saturator containing liquid phase formic acid at 15ºC. Thus, the concentration of HCOOH in the gas phase was related to the vapor pressure of HCOOH at both working temperature and pressure conditions. This concentrated HCOOH/Ar flow was further mixed with an additional Ar flow to obtain the required HCOOH concentration at the working flow rate, corresponding to a weight hourly

space velocity (WHSV) of 4.24 h^{-1}. In-Flow Bronkhorst flow meter (Bronkhorst® High-Tech, the Netherlands) allowed the control of the formic acid-containing air flow, while the main Ar carrier flow was controlled via a Brooks 5850 mass flow meter.

Control tests performed by contacting directly the catalyst bed with a measure thermocouple showed a temperature increase lower than +3°C regardless of the incident irradiance, and independently of the presence or absence of reactant flow.

The photo-/thermo catalytic behavior was obtained by on-line quantification of the outlet flow using a R3000A gas micro-chromatography (SRA instruments), equipped with micro-TCDs, and allowing the quantification of HCOOH, H_2, O_2, CO, CO_2 and organics on 5A molecular sieve, OV1, PoraPlotQ and Stabilwax columns.

Photocatalytic Degradation of 4-chlorophenol

The photocatalytic degradation of 4-chlorophenol measurements were performed in a batch beaker-type glass reactor under UV-A light irradiation (Philips 24 W/10/4P lamps, 60 W/m^2; λ_{max} = 365 nm) at room temperature using 4-chlorophenol as model substrate. In a typical experiment, 100 mg of the catalyst was suspended in 100 mL of a 20 ppm 4-chlorophenol solution and first stirred at 350 rpm in the dark for 1 h to reach the adsorption-desorption equilibrium prior to irradiation. The 4-chlorophenol degradation was followed by UV-Vis spectrophotometry by monitoring the disappearance of the main 4-chlorophenol absorption peak at λ = 225 nm. Samples were taken at each time interval and filtered by using porosity filters (Aireka Cells) with 0.20 μm pore size to remove the catalyst.

Supporting information S2: X-ray diffraction

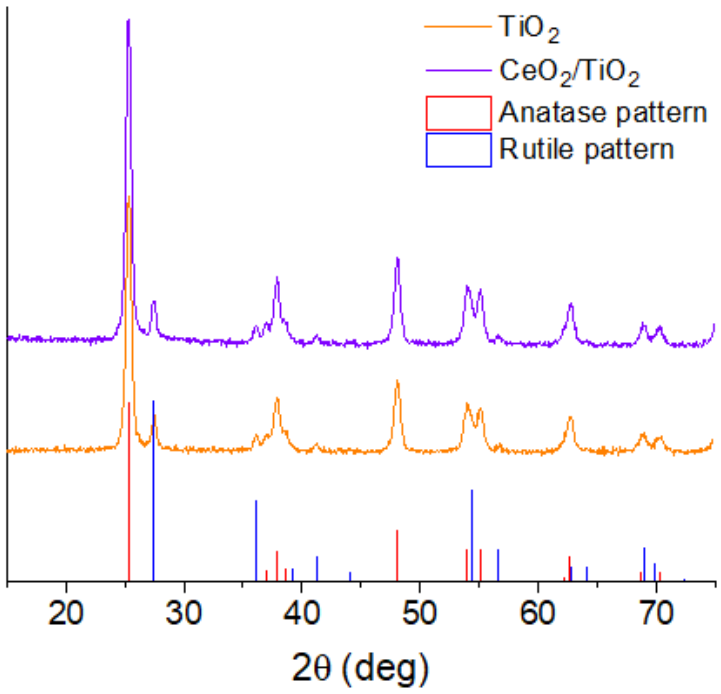

Fig. S2: XRD patterns of the TiO_2 and CeO_2/TiO_2 supports, compared with theoretical diffractograms corresponding to TiO_2 Anatasa and Rutile phases.

Supporting information S3: X-ray photoelectron spectroscopy of CeO_2/TiO_2 support

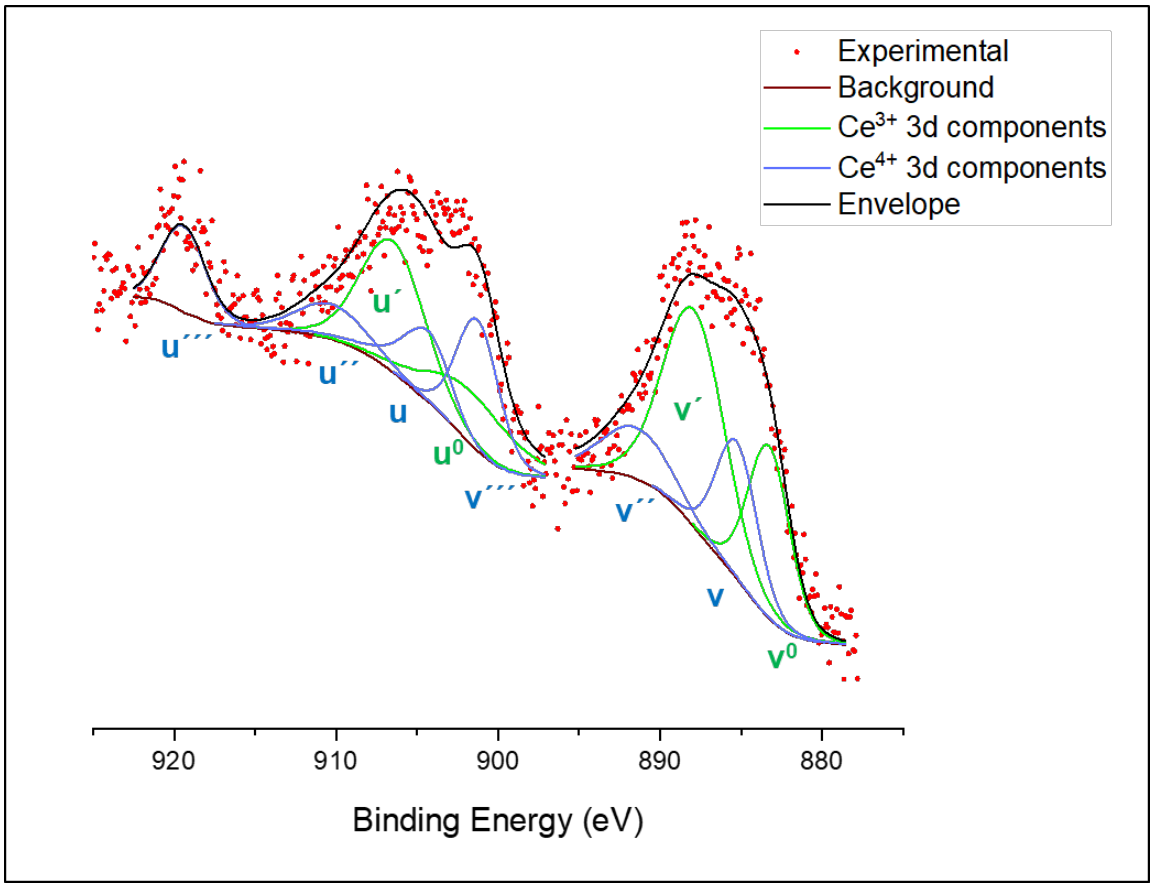

Fig. S3: XPS spectra of Ce 3d core orbitals recorded for the CeO_2/TiO_2 support. The profile has been deconvoluted to fit the Ce^{3+} and Ce^{4+} components.

Supporting information S4: Electron microscopy characterization of highly-dispersed ceria

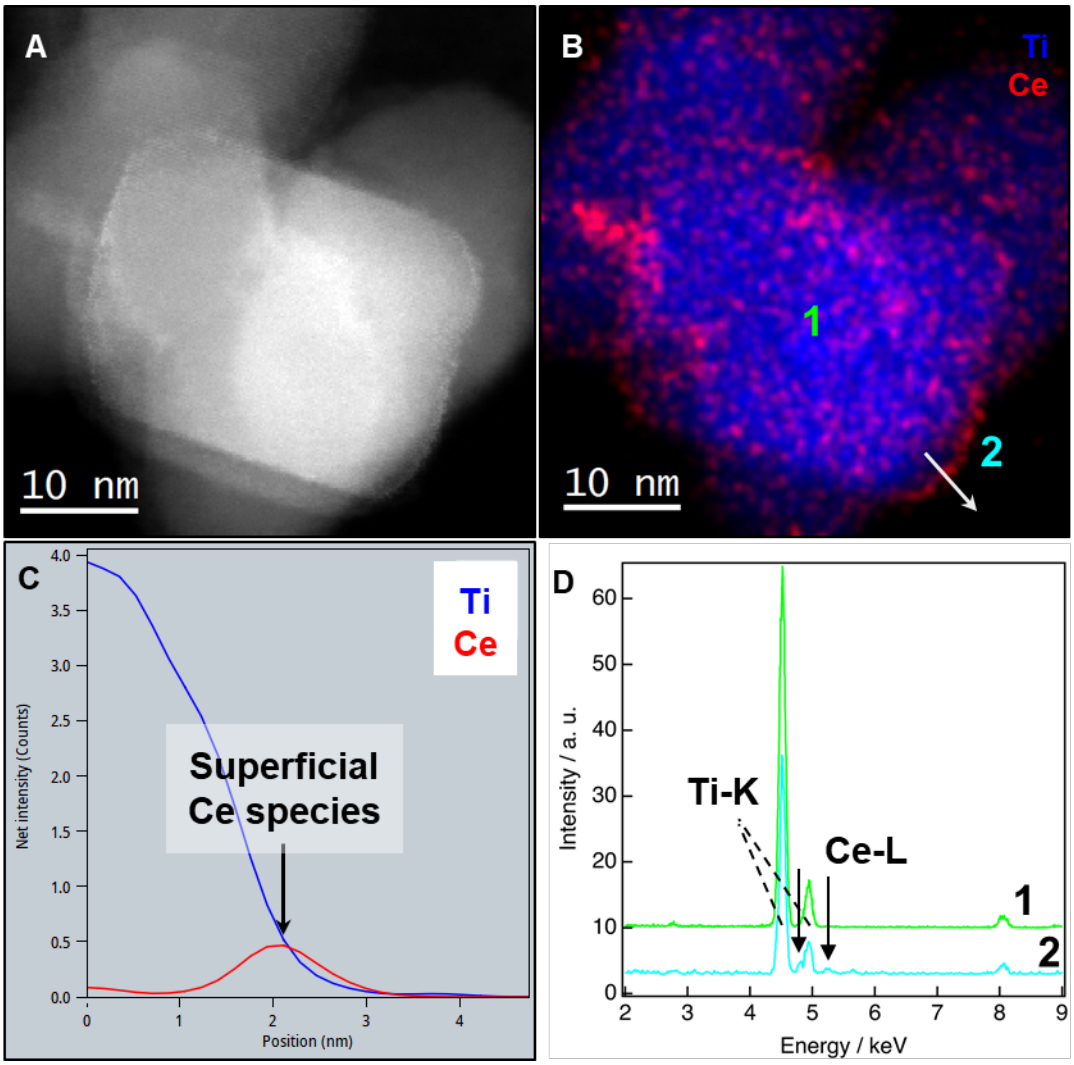

Fig. S4: Characterization of superficial Ce-based species. A, B) Representative HAADF and XEDS elemental map illustrating the CeO_x dispersion on the CeO_2/TiO_2 sample. C) Profile registered across the white arrow, which points out the presence of a high concentration of CeO_x along the surface. D) XEDS spectra extracted from positions marked as 1 and 2, confirming the superficial distribution of CeO_x at the surface of the TiO_2 crystals.

Supporting information S5: Ru photodeposition

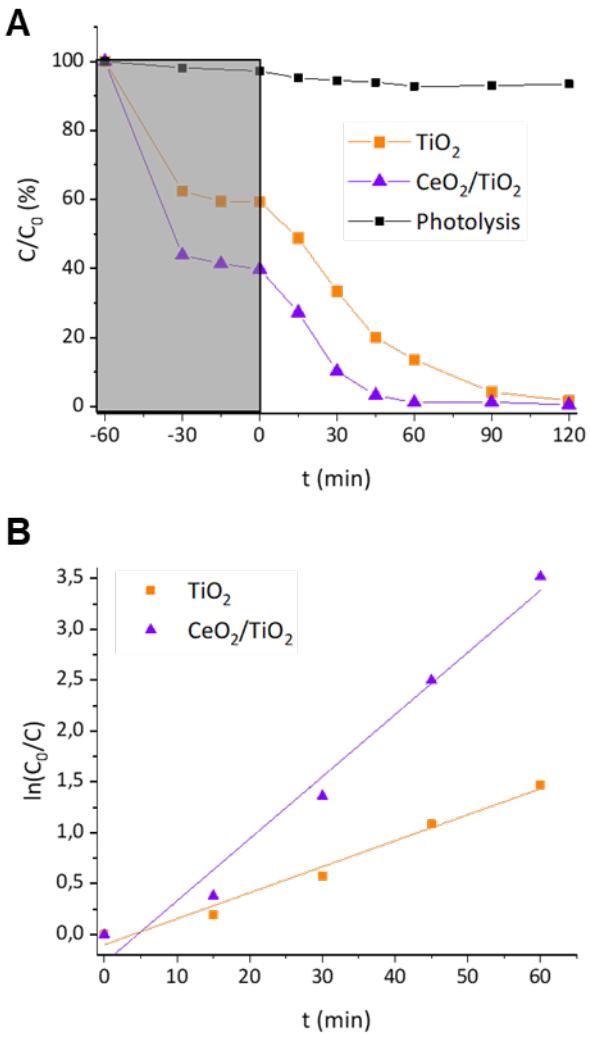

Fig. S5: Solar light-driven photo-assisted synthesis experiments. A) Disappearance of the Ru precursor as a function of the illumination time when the active Ru phase is deposited on the TiO_2 and CeO_2/TiO_2 supports. B) Fitting of the linear transform $\ln(C_0/C)$ to a first-order kinetic rate law.

Supporting information S6: X-ray photoelectron spectroscopy of photodeposited Ru

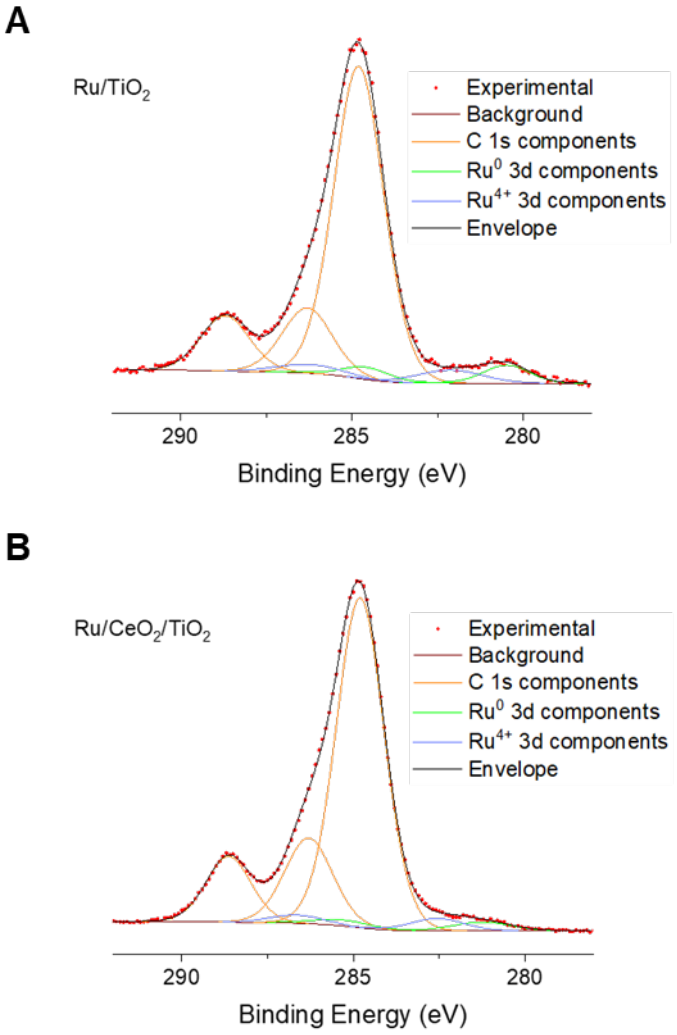

Fig. S6: XPS spectra of Ru 3d and C 1s core orbitals recorded for (A) Ru/ TiO_2 and (B) $Ru/CeO_2/TiO_2$ catalysts.

Supporting information S7: Photodegradation of 4-chlorophenol

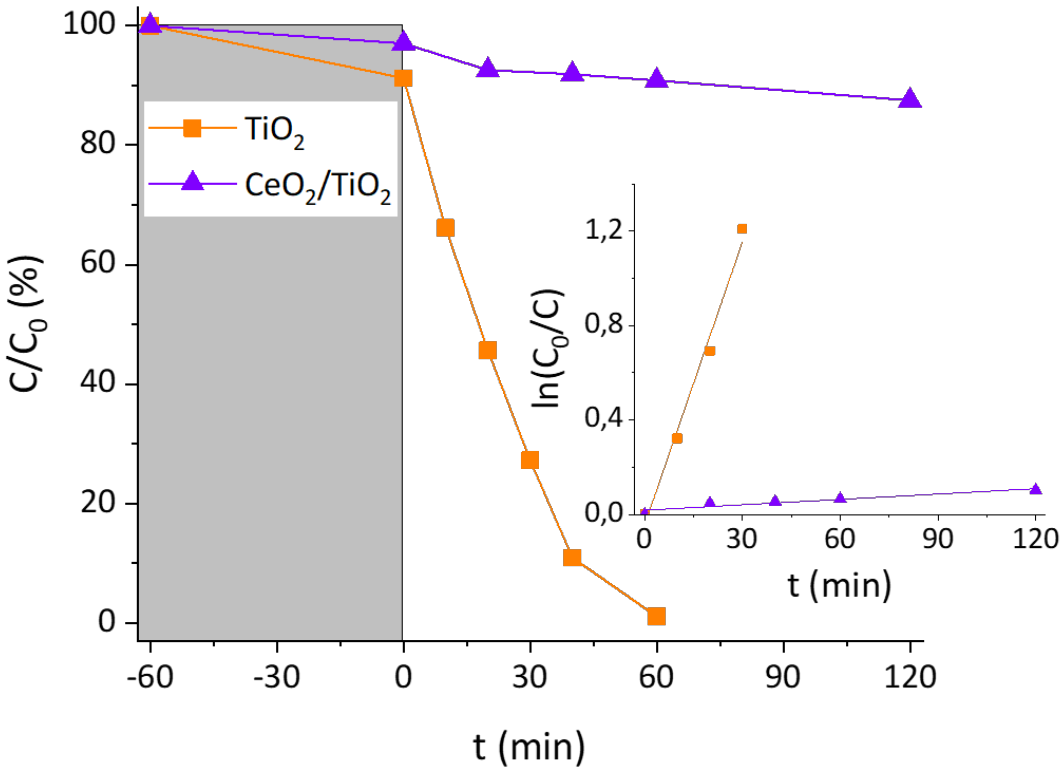

Fig. S7. 4-Chlorophenol photodegradation kinetics on TiO_2 and CeO_2/TiO_2 under UV-A light.